

RESEARCH ARTICLE

10.1002/2013JB010840

Key Points:

- Density structure along the Mendocino Fracture Zone is estimated
- The occurrence of small-scale convection across the fracture zone is suggested

Correspondence to:

C. Cadio,
cecilia.cadio@yale.edu

Citation:

Cadio, C., and J. Korenaga (2014), Resolving the fine-scale density structure of shallow oceanic mantle by Bayesian inversion of localized geoid anomalies, *J. Geophys. Res. Solid Earth*, 119, 3627–3645, doi:10.1002/2013JB010840.

Received 12 NOV 2013

Accepted 20 MAR 2014

Accepted article online 28 MAR 2014

Published online 10 APR 2014

Resolving the fine-scale density structure of shallow oceanic mantle by Bayesian inversion of localized geoid anomalies

C. Cadio¹ and J. Korenaga¹¹Department of Geology and Geophysics, Yale University, New Haven, Connecticut, USA

Abstract We present a new approach to estimate the density structure of shallow oceanic mantle by inversion of localized geoid anomalies. Our method is based on Bayesian statistics and is implemented by combining forward modeling with Markov Chain Monte Carlo sampling. The inherent nonuniqueness of such inversion is reduced by using spectral localization, reference models, and a priori bounds on the amplitude of density perturbations expected within the convecting mantle. We apply this approach to the geoid anomalies around the Mendocino Fracture Zone that have recently been revealed by wavelet analysis. The depth and vertical extent of density anomalies derived from our inversion indicate that they are intimately related to the structure of the lowermost lithosphere. The amplitude of density perturbations and their spatial organization suggest the occurrence of small-scale convection induced by a lateral temperature gradient across the fracture zone. As its applicability is not limited to the vicinity of fracture zones, the new inversion method should allow us to resolve the fine-scale density structure of shallow oceanic mantle beneath the world's oceans.

1. Introduction

As oceanic lithosphere corresponds to the top boundary layer of mantle convection, its gross density structure reflects how the convecting mantle is cooled near the surface. Also, during its long journey from mid-ocean ridges to subduction zones, its basal morphology can be perturbed by interaction with upwelling mantle plumes [e.g., Ribe and Christensen, 1994; Phipps Morgan et al., 1995; Zhong and Watts, 2002] as well as by delamination due to small-scale convection [e.g., Richter and Parsons, 1975; Davaille and Jaupart, 1994; Korenaga and Jordan, 2003]. The fine-scale structure of oceanic lithosphere thus attests to a variety of dynamical processes in the mantle, and delineating it would bring us to a better understanding of geodynamics and mantle rheology.

In this regard, a recent wavelet analysis of the geoid data around the Mendocino Fracture Zone is noteworthy, because it has revealed 100 to 200 km scale anomalies, which substantially deviate from any of the reference evolution models of oceanic lithosphere and call for prominent density anomalies at relatively shallow depths [Cadio and Korenaga, 2012]. Local geoid anomalies along fracture zones have long been recognized [Driscoll and Parsons, 1988; Marty and Cazenave, 1988; Wessel and Haxby, 1989; Freedman and Parsons, 1990]; while some of them were attributed to small-scale convection [e.g., Robinson et al., 1988], however, none of them have been thoroughly analyzed. Yet these small-scale geoid anomalies could carry important information regarding the fine-scale density structure (and thus dynamics) of oceanic lithosphere and asthenosphere.

Constraining the fine-scale structure of shallow oceanic mantle is difficult by traditional seismological methods because of incomplete ray coverage or limited data resolution. At a regional scale, active source seismology with a dense array of ocean bottom seismometers can provide high-resolution images, but only down to the base of the crust. Surface wave tomography can image deeper structure at a global scale, but with much lower resolution. Based on the surface wave tomography of the Pacific mantle, for example, Ritzwoller et al. [2004] have suggested that old lithosphere does not follow half-space cooling, but the spatial resolution of their tomography does not allow them to exclude the effect of hotspot chains and oceanic plateaus, which are so densely populated on the old seafloor in the Pacific [Korenaga and Korenaga, 2008]. In terms of spatial resolution, surface observables such as topography and geoid are far superior, and even though the interpretation of any potential field is fundamentally nonunique [e.g., Blakely, 1995], such nonuniqueness may be substantially reduced by spectral localization techniques, the availability of reference models, and a priori bounds on the amplitude of geologically plausible perturbations. In particular,

the geoid anomaly depends on the depth-weighted integral of density anomalies [Ockendon and Turcotte, 1977], thereby being sensitive to perturbations in the lower portion of the lithosphere unlike other observable quantities such as seafloor depth and heat flow. Combined with ground-based and altimeter-derived measurements, high-quality data from the space gravity mission Gravity Recovery and Climate Experiment (GRACE) now allow us to accurately map the static geoid on the entire surface of Earth with a lateral resolution on the order of 50 km [e.g., Förste et al., 2008].

The main purpose of this paper is to present a new approach to invert the aforementioned small-scale geoid anomalies for the statistical distribution of their source density anomalies in the shallow upper mantle. Our method is based on Bayesian statistics and is implemented by combining forward modeling with Markov Chain Monte Carlo (MCMC) sampling. We apply this approach to published findings around the Mendocino Fracture Zone [Cadio and Korenaga, 2012]. In what follows, we first explain how to process geoid data prior to our inversion, using the Mendocino case as an example. We then describe the inversion procedure and present the statistical representation of density perturbations derived by our MCMC inversion. Finally, we show that this newly derived density distribution can provide useful constraints on the rheology of oceanic mantle.

2. Defining and Localizing Residual Geoid Anomalies

The geoid signal as a whole reflects the mass distribution within the entire Earth, so directly inverting observed geoid anomalies for subsurface density anomalies would suffer from considerable nonuniqueness. We try to minimize the degree of nonuniqueness in two ways, (1) by incorporating our understanding of the standard evolution of oceanic lithosphere and (2) by focusing on the short wavelength components of geoid anomalies with spectral localization. The evolution of oceanic lithosphere is much simpler than that of its continental counterpart, and the first-order characteristics of oceanic lithosphere can be modeled as a function of seafloor age [Parsons and Sclater, 1977; Stein and Stein, 1992; Carlson and Johnson, 1994]. By taking into account such a priori knowledge, we can define residual geoid anomalies, which may be inverted for deviations from the standard evolution model of oceanic lithosphere. Spectral localization further assists this inversion by limiting the depth extent of source density anomalies. In this section, our approach is explained in detail by using the case of the Mendocino Fracture Zone, to make our description concrete, but the approach itself is of more general applicability.

2.1. Residual Geoid Anomalies

The thermal lithosphere gradually thickens as it cools and spreads away from mid-ocean ridges, and the seafloor subsides owing to isostasy [Turcotte and Schubert, 2002]. Seafloor subsidence by isostasy causes the geoid anomalies to decrease gradually with age. Assuming an isostatically compensated lithosphere, therefore, a theoretical geoid can be calculated, and deviations from such a theoretical expectation may be defined as residual geoid anomalies. Analytical solutions for a theoretical geoid exist for the half-space cooling (HSC) model [Haxby and Turcotte, 1978] and the plate model [Haxby and Turcotte, 1978; Parsons and Richter, 1980; Sandwell and Schubert, 1980], but the use of these analytical solutions is equivalent to ignoring any lateral density variations, which is inappropriate especially when considering geoid signals around a fracture zone. As in Cadio and Korenaga [2012], therefore, we calculate a theoretical geoid for the HSC and plate models by numerical integration in the spatial domain. In the study area, which contains the younger part (ages < 60 Ma old) of the Mendocino Fracture Zone (Figure 1), both models yield similar theoretical predictions. For the sake of simplicity, we adhere to the HSC model in this study. The values of thermal parameters used in the theoretical calculation are given by Cadio and Korenaga [2012].

We apply the continuous wavelet transform with spherical Poisson multipole wavelets [Holschneider et al., 2003] to localize the observed geoid and the theoretical geoid, at lateral scales varying from 100 to 500 km. Such analysis provides a detailed description of signals both in spatial and spectral domains. It is constructed from a set of coefficients as defined from the correlation between the signal and a wavelet, at a given spatial scale and position, and thus highlights the signal components at the corresponding scale and position. For instance, at 100 km scale, our wavelet analysis underlines spatial features in the geoid of ~100 km [see Cadio and Korenaga, 2012, Figure 1] in each point of the study area. A best agreement between the observation and the prediction is obtained at the scale of 100 km [Cadio and Korenaga, 2012]. The agreement at this length scale is reasonable because the expected depths of density sources range from the surface to about 100–150 km, which corresponds to the depth extent of oceanic lithosphere.

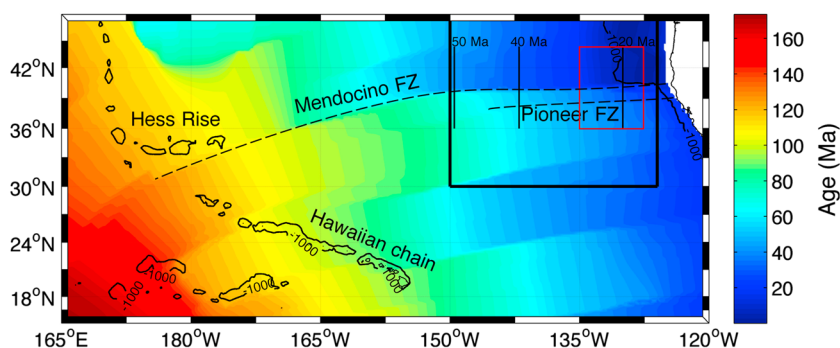


Figure 1. Seafloor age is shown in color for the Northeast Pacific [Müller *et al.*, 2008], with counters for bathymetry. The Mendocino Fracture Zone is located at 40°N and runs from the west coast of North America to the Hess Rise located near the bend of the Hawaii-Emperor seamount chain. The Pioneer Fracture Zone is about 150 km south of the youngest portion of the Mendocino Fracture Zone. The black box represents the study area of Cadio and Korenaga [2012], and the red box is our region of interest in this paper.

As the theoretical geoid is computed based on the HSC model of oceanic lithosphere, its comparison to observations is most appropriate at this short length scale; the spectral localization effectively removes the longer-wavelength signals originating in deeper-mantle processes.

The wavelet coefficients of the observed and theoretical geoid signals at 100 km scale are shown over seafloor younger than 30 Ma old in Figures 2a and 2b, respectively. Though both observations and predictions share a similar overall pattern, they do differ at various places (Figure 2c). In particular, the observed signal around the Mendocino Fracture Zone shows more negative anomalies than theoretically expected, and that around the Pioneer Fracture Zone is barely explained theoretically. The residual geoid anomalies vary with the amplitudes of ~0.5 m (~ 60% of the observed geoid signal at 100 km scale), thus pointing to nontrivial perturbations to the standard lithospheric model, either in topography or in subsurface density structure. The former possibility can be assessed relatively easily, so it is discussed next.

2.2. Correcting for Residual Topography

The standard evolution model of oceanic lithosphere provides not only a theoretical geoid but also a theoretical bathymetry [e.g., Cadio and Korenaga, 2012, equation (11)]. When a theoretical geoid does not match an observed one, a mismatch is likely to exist in bathymetry as well, which is the case for the Mendocino Fracture Zone. Figure 2f shows residual topography, i.e., deviation from the theoretical bathymetry, localized at the scale of 100 km. The amplitude of residual topography is on the order of a few hundred meters. The coherence between the residual geoid and the residual topography is calculated in each point of the study area following the wavelet method developed in Cadio *et al.* [2012] and is shown in Figure 3. Each value of the local coherence is obtained from the geoid and topography wavelet coefficients over a window, the width of which is twice the scale of the wavelet. The significance of the local coherence in the 95% confidence limit is 0.67. By including the effect of the measurement noise on the coherence [Cadio *et al.*, 2012], we thus consider that the geoid and the topography are correlated if the coherence is greater than the lower bound of 0.5. In the study area, the analysis of the local coherence shows that the correlation between the geoid and the topography is weak and does not exceed 0.5 except in a restricted area north of the fracture zone. Nonetheless, it is important to check how much of the residual geoid can be explained by the residual topography. To this end, an isostatic geoid is calculated from the residual topography assuming Airy compensation as follows [Haxby and Turcotte, 1978]:

$$N_{\text{Airy}} = \frac{\pi G}{g} (\rho_c - \rho_w) \left\{ 2Hh + \left(\frac{\rho_m - \rho_w}{\rho_m - \rho_c} \right) h^2 \right\}, \quad (1)$$

where G is the gravitational constant, g is the mean surface gravity, H is the thickness of reference oceanic crust, h is residual topography, and ρ_w , ρ_c , and ρ_m are, respectively, the density of seawater, crust, and mantle. The isostatic geoid shown in Figure 2e is of amplitude considerably lower than that of the residual geoid, indicating that the majority of the residual geoid is caused by subsurface density anomalies. The residual geoid after subtracting this isostatic geoid (Figure 2d) will be used as input for inversion (see section 3).

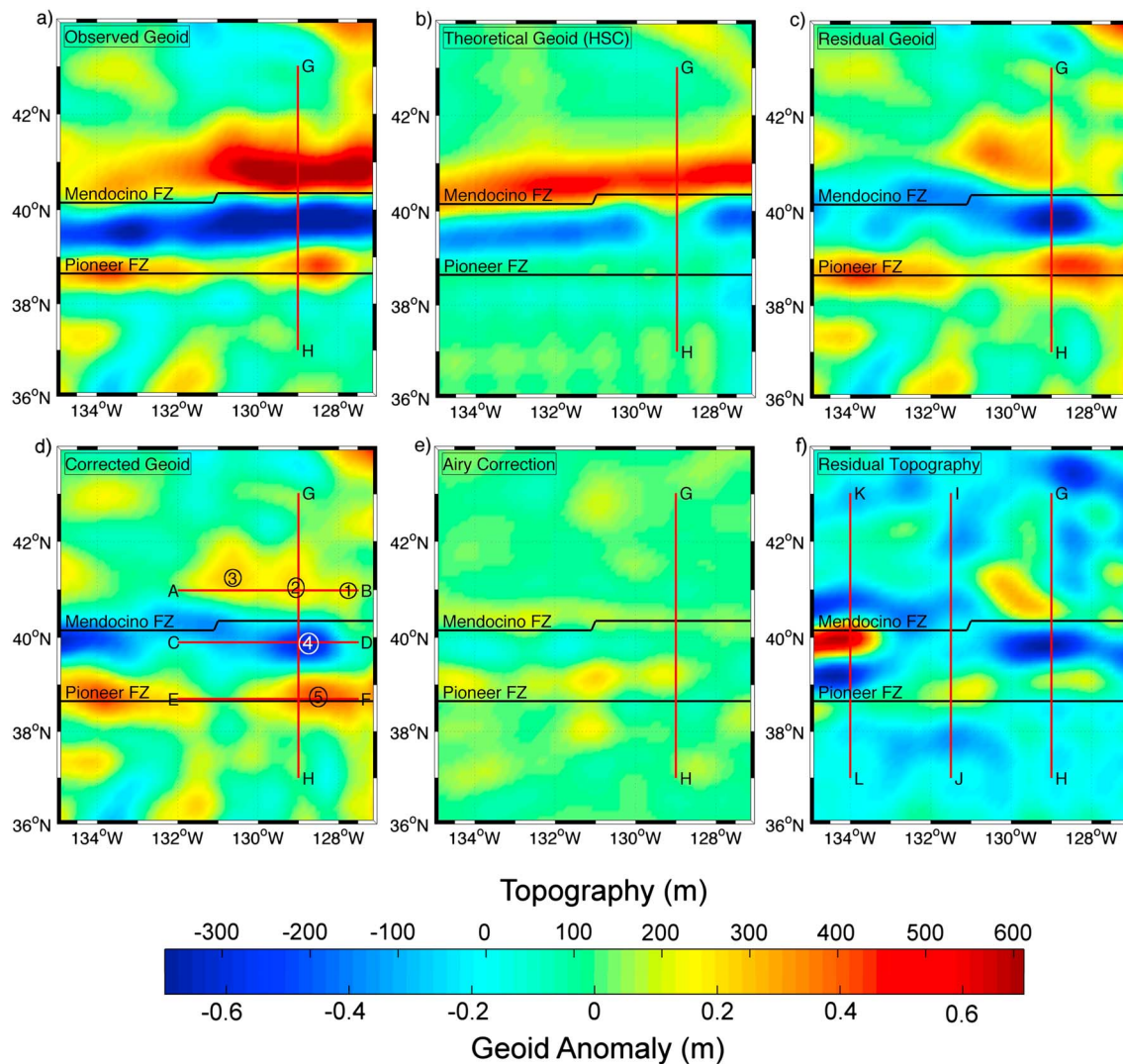


Figure 2. Localized geoid and topography anomalies around the Mendocino Fracture Zone (with seafloor ages of ~20–30 Ma old). (a) Observed geoid, (b) the theoretical geoid based on the HSC model, and (c) difference between these two, all at the scale of 100 km. (d) Localized geoid anomalies after Airy correction. Small-scale anomalies numbered from 1 to 5 are considered in this study. (e) Correction for the effect of this residual topography with the assumption of Airy isostatic compensation. (f) Localized residual topography, defined as the difference between the observed and theoretical topography from the HSC model, at 100 km scale.

In the vicinity of a fracture zone, further consideration is needed. If a fracture zone is sufficiently strong to couple juxtaposed lithospheric segments, differential subsidence across the fracture zone could elastically deflect the lithosphere, producing a ridge on the younger side and a trough on the older side [Sandwell and Schubert, 1982; Sandwell, 1984]. As such flexural topography is not isostatically compensated, it contributes to geoid anomalies differently from the isostatic geoid considered above. In our study area, the possibility of flexural topography does not seem to be very important because the characteristic ridge-trough pair is not consistently observed along the Mendocino Fracture Zone (Figure 2f). It is still useful, however, to compute flexural topography and corresponding geoid signal for quantitative discussion and also for future reference.

Flexural topography, w , can be estimated by solving the equation of a thin elastic plate model [Turcotte, 1979]:

$$D \frac{d^4 w}{dx^4} + g(\rho_m - \rho_w)w = P(x), \quad (2)$$

where D is flexural rigidity, and P is the pressure exerted on the elastic plate. The pressure is given by Sandwell [1984, equation (8)], and we assume that the flexural rigidity is constant across the fracture

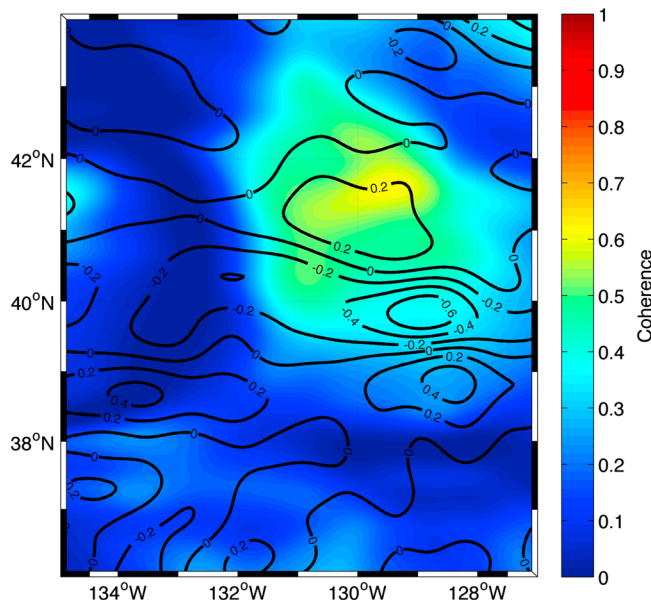


Figure 3. Map of the local wavelet coherence in the study area (see the red box in Figure 1) at 100 km scale, with counters for residual geoid anomalies.

geoid can then be calculated in the wave number domain using only the first term in the expansion of Parker [1972]:

$$N(k) = \frac{2\pi GW(k)(\rho_m - \rho_w) \exp(-|k|d)}{g|k|}, \quad (4)$$

where k is the wave number, d is the mean depth, and $N(k)$ and $W(k)$ are, respectively, the Fourier transform of the geoid and the topography. These functions are transformed back into the space domain by using the inverse Fourier transform. The continuous wavelet transform is then applied at the scale of 100 km.

Figures 4a–4c show the predicted flexural topography across the Mendocino Fracture Zone when the age of the younger side is 5, 10, and 15 Ma (along profiles GH, IJ, and KL in Figure 2f). Though the predicted flexural topography has an amplitude similar to that of the residual topography, these two types of topography are characterized by different patterns. In the study area, the fracture zone seems too weak to couple the two lithospheric segments and cause significant flexure, which is in agreement with the study of Hall and Gurnis [2005] on the strength of Pacific fracture zones. With a weak fracture zone, the two segments can act as uncoupled blocks that subside isostatically. A similar comment can be made for the comparison between the residual geoid (before the Airy correction) and the flexural prediction (Figure 4d).

Given their spatial scales and weak correlation with residual topography, localized residual geoid anomalies may be safely regarded to originate in perturbations to the density structure of normal oceanic lithosphere. We choose to study five of these small-scale anomalies, which are numbered from 1 to 5 in Figure 2d. The geographical distribution of these anomalies allows us to explore the structure of oceanic lithosphere, both along and across the Mendocino Fracture Zone. A detailed analysis of their spectral contents is however necessary to ensure that these anomalies are of shallow mantle origin. When studying the variations of the wavelet coefficients as a function of scale in the area of anomaly, a local maximum of amplitude is observed at the characteristic scale of the density anomaly. For each of these five anomalies, we thus calculate a local wavelet spectrum at scales varying from 50 to 500 km (Figure 5). Such spectrum, at each scale, contains the mean wavelet coefficient amplitude over the area of anomaly and thus allows the identification of minima/maxima in the geoid at specific scales. We identify an extremum at 100 km for all of the anomalies, indicating that this spatial scale is the characteristic scale of a source density perturbation [Cadio *et al.*, 2011].

zone, with the value appropriate to the age t of the lithosphere on the younger side [Sandwell and Schubert, 1982]:

$$D = \frac{2E(\kappa t)^{3/2}}{3(1 - \nu^2)} \left[\operatorname{erfc}^{-1} \left(\frac{T_m - T_e}{T_m - T_s} \right) \right]^3, \quad (3)$$

where E is Young's modulus, ν is Poisson's ratio, κ is the thermal diffusivity, $\operatorname{erfc}(x)$ is the complementary error function, and T_m , T_s , and T_e are, respectively, the mantle temperature, the surface temperature, and the stress relaxation temperature. Using the age of the younger side leads to an overestimate of flexural topography mainly on the older side of the fracture zone, so our estimate represents an upper limit. Equation (2) may be solved by taking its Fourier transform, and a corresponding

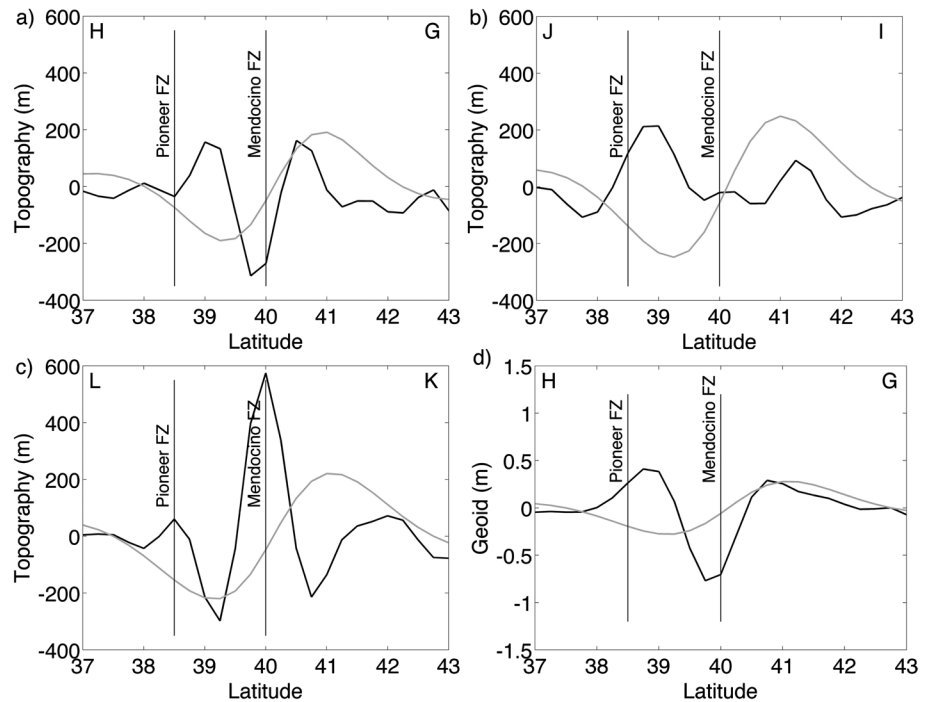


Figure 4. Residual topography (black) and predicted flexural topography (grey), at 100 km scale and along the profiles (a) GH, (b) IJ, and (c) KL (see Figure 2f). (d) Same as Figure 4a but in terms of corresponding geoid anomalies.

3. Inversion Methodology

3.1. Bayesian Strategy

We employ a Bayesian framework to formulate our inverse method [e.g., Tarantola, 1987; Mosegaard and Tarantola, 1995]. In this framework, the a posteriori probability for a model vector \mathbf{m} is given as

$$\rho(\mathbf{m}) = k f(\mathbf{m}) L(\mathbf{m}), \tag{5}$$

where k is a normalization constant, $f(\mathbf{m})$ is the a priori probability, i.e., the quantification of prior information about \mathbf{m} , and $L(\mathbf{m})$ is the likelihood function, which is a measure of misfit between observations and predictions from \mathbf{m} . The a priori probability can take a simple form, e.g., $f(\mathbf{m}) = c$ (c being a positive constant) if all of model parameters are within their prescribed bounds, and $f(\mathbf{m}) = 0$ otherwise. We define $L(\mathbf{m})$ using the cost function $\chi^2(\mathbf{m})$ as

$$L(\mathbf{m}) = \exp\left(-\frac{1}{2} \chi^2(\mathbf{m})\right), \tag{6}$$

where

$$\chi^2(\mathbf{m}) = \sum_{i=1}^N \frac{(\Delta N_i^{obs} - \Delta N_i^{pre}(\mathbf{m}))^2}{\sigma_i^2}. \tag{7}$$

Here ΔN_i^{obs} and $\Delta N_i^{pre}(\mathbf{m})$ denote, respectively, observed and predicted geoid anomalies for the i th datum, σ_i^2 is a corresponding data variance, and N is the total number of data. The comparison of observed and predicted anomalies is via the wavelet transform at the scale of 100 km. As the EIGEN-GL04C geoid model has an

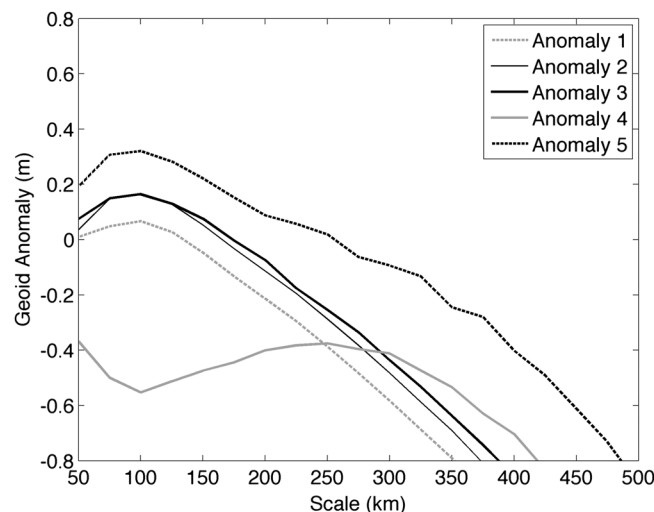


Figure 5. Local wavelet spectra of the five investigated geoid anomalies for scales varying between 50 and 500 km.

accumulated error of ~ 0.1 m at 100 km resolution, we assign this value to σ_i . The normalization constant k is determined so that

$$\int_{\mathcal{M}} \rho(\mathbf{m}) d\mathbf{m} = 1, \tag{8}$$

where \mathcal{M} denotes the entire model space. In the Bayesian framework, solving the inverse problem becomes equivalent to calculating the model mean and variance by evaluating the following integrals

$$\text{mean}\{\mathbf{m}\} = \int_{\mathcal{M}} \mathbf{m} \rho(\mathbf{m}) d\mathbf{m}, \tag{9}$$

and

$$\text{var}\{\mathbf{m}\} = \int_{\mathcal{M}} (\mathbf{m} - \text{mean}\{\mathbf{m}\})^2 \rho(\mathbf{m}) d\mathbf{m}, \tag{10}$$

together with equations (5)–(8).

Evaluating the above multidimensional integrals, however, can be very time consuming or even impractical when the number of model parameters is not small. MCMC is a popular choice to obtain approximate results in an efficient manner [e.g., Liu, 2001; Robert and Casella, 2004] (see section 3.4). In addition to this common issue in Bayesian-based inverse methods, we also need to cope with the fundamental nonuniqueness of potential field data. Our strategy is to restrict ourselves to simple source parameterization (see section 3.2) and to incorporate our geological understanding (see section 3.3).

3.2. Forward Modeling and Parameterization

We choose to approximate subsurface density perturbations as a collection of prisms. To be more specific, for each of the small-scale geoid anomalies identified in Figure 2d, a corresponding source body is assumed to be a right rectangular prism with constant density perturbation, $\delta\rho$ (Figure 6). This particular choice of a source body is rather arbitrary. It could be an ellipsoid instead, and the density could gradually change within a source body. Because of the inherent nonuniqueness associated with a static potential field, however, we regard that such details are immaterial. Our aim is to test whether we can place useful (albeit likely to be crude) bounds on subsurface density distribution, and the use of a right rectangular prism is deemed to suffice.

The geoid contribution of such a rectangular prism, observed at point P , can be computed analytically in the Cartesian coordinates as follows [e.g., Nagy et al., 2000]:

$$\Delta N(P) = \frac{G\delta\rho}{g} \int_{x_1}^{x_2} \int_{y_1}^{y_2} \int_{z_1}^{z_2} (R - S) dx dy dz, \tag{11}$$

where

$$R = xy \ln(z + r) + yz \ln(x + r) + zx \ln(y + r), \tag{12}$$

$$S = \frac{z^2}{2} \arctan\left(\frac{xy}{zr}\right) + \frac{x^2}{2} \arctan\left(\frac{yz}{xr}\right) + \frac{y^2}{2} \arctan\left(\frac{xz}{yr}\right), \tag{13}$$

$$r = \sqrt{x^2 + y^2 + z^2}, \tag{14}$$

$$x_j = X_j - X_p, \quad y_j = Y_j - Y_p, \quad z_j = Z_j - Z_p, \tag{15}$$

$(X_j, Y_j, Z_j)_{j=1,2}$ are the prism coordinates and (X_p, Y_p, Z_p) denotes the location of the observation point P . These relations are only appropriate for relatively small study areas where a flat Earth approximation can be used. As independent parameters for a source body, we use the following: its density $\delta\rho$, depths to the top Z_1 and the bottom Z_2 , and its lateral extents δX and δY (Figure 6). In addition, we define a sixth parameter, θ , which accounts for the orientation of the prism. Equation (11) requires the prism to be bounded by planes parallel to the coordinate planes, but the effect of varying θ can easily be achieved by rotating a geoid signal about its center. Each prism model is thus described by a set of six parameters, i.e., $\mathbf{m} = \{\delta\rho, \delta X, \delta Y, Z_1, Z_2, \theta\}$. The space spanned by all possible models is denoted by \mathcal{M} . To be consistent with the residual geoid anomalies to be modeled, theoretical geoid anomalies are also passed through the wavelet transform with the scale of 100 km.

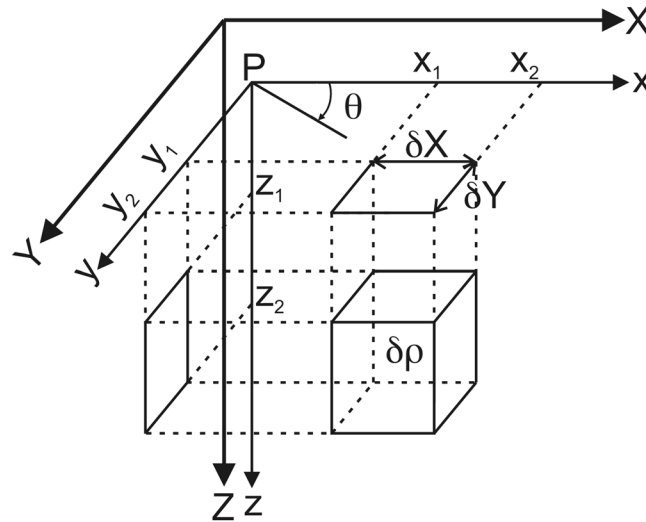


Figure 6. Notation used for the definition of a prism [after Nagy *et al.*, 2000].

of perturbations may be extended to $\sim 500^\circ\text{C}$ by considering lithospheric delamination (or erosion) by small-scale convection and plume impingement. Corresponding density perturbations are up to $\pm 50 \text{ kg m}^{-3}$. Likely chemical heterogeneities in the upper mantle would not lead to greater density perturbations; the Mg# of mantle rocks is usually in the range of 87 to 93 [e.g., Boyd, 1989; Lyubetskaya and Korenaga, 2007], the extrema of which correspond to rather extreme fertilization and depletion events, respectively, and the compositional dependency of mantle density is approximately $-15 \text{ kg m}^{-3}/\text{Mg\#}$ [Lee, 2004].

Second, based on potential field theory [e.g., Blakely, 1995], the lateral extent of the prism cannot exceed the spatial extent of the geoid anomaly under consideration. Also, the width of the geoid anomaly is tightly related to the maximum depth of the density anomaly since a given wavelength corresponds to a maximum penetration depth. Here the Poisson multipole wavelets are of special interest since their scale parameter is related to the maximal depth of the geoid equivalent source [see Holschneider *et al.*, 2003, equation (35)]. At 100 km scale, for example, the wavelet analysis limits us to the density anomalies from the surface down to about 150 km. The ranges explored for our model parameters are summarized in Table 1.

3.4. Sampling the Model Space

Having described the model vector (see section 3.2) and its bounds (see section 3.3), we are now ready to implement an MCMC procedure to evaluate the integrals of equations (9) and (10).

Our implementation is based on the Metropolis-Hastings algorithm [Metropolis *et al.*, 1953; Hastings, 1970]. We choose to express a priori model constraints as upper and lower limits on model parameters $\mathbf{m} = \{m_k | k = 1, 2, \dots, 6\}$, i.e.,

$$m_k^l \leq m_k \leq m_k^u. \tag{16}$$

By keeping a Markov chain within these bounds, model sampling is automatically restricted where $f(\mathbf{m}) = c$ ($c > 0$) [e.g., Mosegaard and Tarantola, 1995]; that is, the influence of a priori probability $f(\mathbf{m})$ in equation (5) is properly taken into account. Our MCMC procedure is as follows:

1. Initialization. Draw six random numbers, r_k , from the interval $[0, 1]$ to set the initial model, \mathbf{m}_0 , as

$$m_{0,k} = m_k^l + r_k(m_k^u - m_k^l), \tag{17}$$

for $k = 1, 2, \dots, 6$. For a pseudo-random number generator, we use Numerical Recipes' `ran2` function [Press *et al.*, 1992]. Calculate the corresponding probability, $\rho(\mathbf{m}_0)$.

3.3. Further A Priori Constraints

By assuming a simple source body, we are able to reduce the number of model parameters to just six. We can further limit the model space to be explored by incorporating our understanding of mantle dynamics and potential field theory.

First of all, a priori bounds on density perturbation may be obtained by considering how density can be modified by thermal and chemical processes in the convecting mantle. Temperature variations in asthenosphere inferred from petrological [e.g., Herzberg *et al.*, 2007] and geophysical [e.g., Sleep, 1990] studies are 100 to 300°C around the normal mantle temperature. This range

Table 1. Definitions of Parameters and Their Values (or A Priori Ranges)

Parameter	Definition	Value
α	thermal expansion coefficient	$3.1 \times 10^{-5} \text{ K}^{-1}$ ^a
d	mean depth	2600 m
$\delta\rho$	prism density	$-50\text{--}50 \text{ kg m}^{-3}$
δX	lateral extent in x direction	10–200 km
δY	lateral extent in y direction	10–200 km
E	Young's modulus	$6.5 \times 10^{10} \text{ Pa}^a$
g	mean surface gravity	9.81 m s^{-2}
G	gravitational constant	$6.67 \times 10^{-11} \text{ m}^3 \text{ kg}^{-1} \text{ s}^{-2}$
H	thickness of reference oceanic crust	6 km
κ	thermal diffusivity	$8 \times 10^{-7} \text{ m}^2 \text{ s}^{-1}$ ^a
ν	Poisson's ratio	0.25 ^a
ρ_c	crustal density	2900 kg m^{-3}
ρ_m	mantle density	3330 kg m^{-3} ^a
ρ_w	seawater density	1025 kg m^{-3} ^a
T_e	stress relaxation temperature	450°C^a
T_m	mantle temperature	1365°C^a
T_s	surface temperature	0°C^a
θ	prism orientation	0–179°
Z_1	prism top	1–100 km
Z_2	prism bottom	11–200 km

^aFrom Sandwell and Schubert [1982].

2. Random perturbation. Pick another six random numbers, $\gamma_{1,k}$, from the interval $[-1, 1]$ to set a trial model \mathbf{m}' as

$$m'_k = m_{0,k} + \gamma_{1,k} \Delta m_k, \quad (18)$$

where Δm_k is the maximum amplitude of perturbation for the k th parameter (see section 4.1). Calculate $\rho(\mathbf{m}')$.

3. Acceptance or rejection. If $\rho(\mathbf{m}') > \rho(\mathbf{m}_0)$, \mathbf{m}' is a better model than \mathbf{m}_0 , so we accept this perturbed model as the next model. If $\rho(\mathbf{m}') \leq \rho(\mathbf{m}_0)$, on the other hand, we draw one random number, γ_2 , from the interval $[0, 1]$. If $\gamma_2 < \rho(\mathbf{m}')/\rho(\mathbf{m}_0)$, go to the next step. Otherwise, start over from step 2.
4. Model update. Save the initial model \mathbf{m}_0 and redefine it with \mathbf{m}' . Until the maximum number of iteration is reached, go back to step 2.

The ability of the Metropolis algorithm to efficiently explore the model space may be seen in Figure 7. The distribution of normalized χ^2 (i.e., χ^2/ν where ν is the degrees of freedom) shows that this guided random walk spends most of its time within the high-probability region of the model space. Normalized χ^2 is calculated on a restricted area around the geoid anomaly. The degrees of freedom can be approximated by the number of wavelet oscillations without overlap in this restricted area. As the anomalies have been handled separately, the ν value varies and is 6, 1, 4, 5, and 8 for the anomalies 1 to 5, respectively. In order to demonstrate how the above MCMC procedure works and to help the interpretation of results in the next section, we first consider a synthetic example. The results are described in Appendix A.

4. Results

4.1. Convergence of MCMC Sampling

Before describing our inversion results in terms of subsurface density distribution, we need to ensure that the model space has been extensively explored by testing the convergence of our MCMC sampling. A Markov chain may be said to be converged if it has visited all important models (i.e., those with high a posteriori density probabilities). The number of iterations necessary to reach this situation depends heavily on how random walk is simulated. In particular, the perturbation size to create a trial move must be carefully chosen. It must be small enough so that successive moves do not result in drastic model changes, which usually result in rejecting most trial moves, but also large enough to avoid being trapped near a local minimum for a long time. With some trial and error, we chose to set the maximum amplitude of perturbation as $\Delta m_k = 0.075(m_k^U + m_k^L)$ for all model parameters.

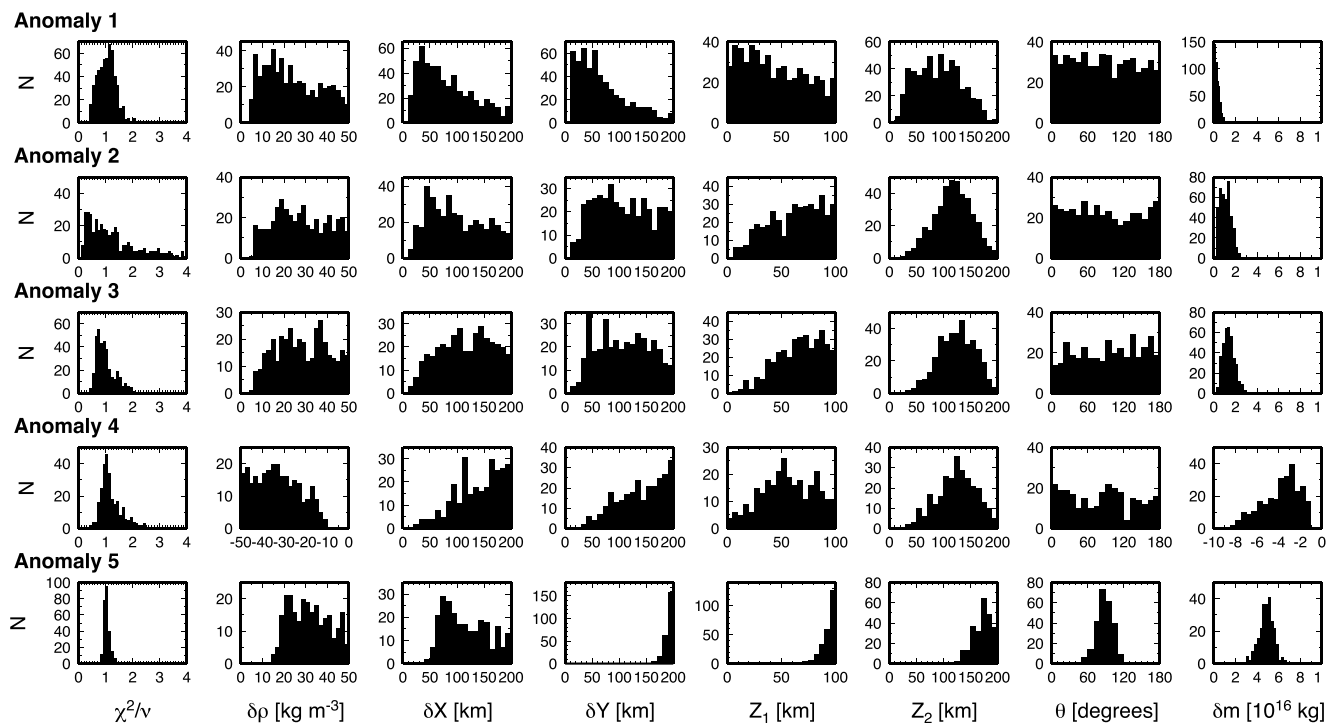


Figure 7. Histograms of resampled MCMC solutions from five simulations corresponding to different observed geoid anomalies.

Because each perturbation is of small amplitude, successive models in a Markov chain are highly correlated. To collect statistically independent models, we calculate for all model parameters the autocorrelation function, which is the cross correlation of a given Markov chain with itself, but shifted by a certain number of steps called “lag” (Figure 8). These autocorrelation functions invariably decrease with an increasing lag and become virtually zero within a lag of ~700–1000. We thus resample every 10^3 models to gather uncorrelated models. We run MCMC until the number of iterations reaches 10^6 so that the number of resampled solutions is 10^3 . To ignore bad models in the early stage, we discard the first 10^3 samples before resampling.

We test for convergence by comparing two parallel runs that start at different initial models. We calculated the mean and standard deviation of model parameters for each MCMC run, and as shown in Table 2, the results of those runs are very similar. We are thus reasonably confident in having explored the entire model space after 10^6 iterations, and the distribution of our MCMC solutions should correspond closely to the a posteriori probability distribution $\rho(\mathbf{m})$.

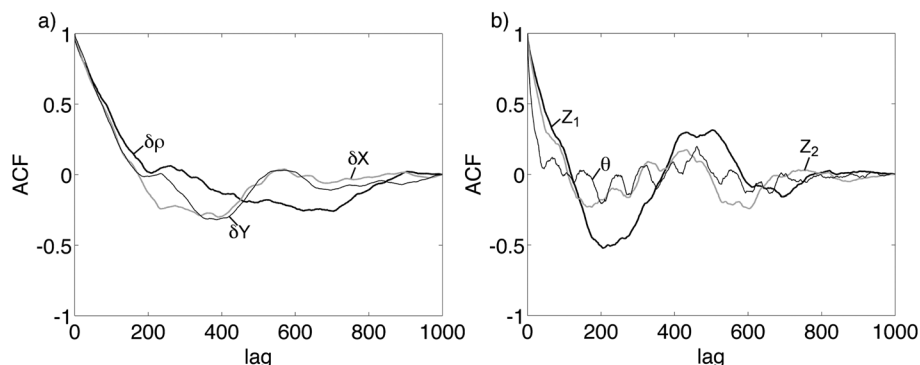


Figure 8. Autocorrelation function (ACF) for the MCMC run for geoid anomaly 1. (a) Prism density contrast ($\delta\rho$) and lateral extents (δX and δY). (b) Top depth (Z_1), bottom depth (Z_2), and prism orientation (θ).

Table 2. Mean and Standard Deviation of Model Parameters Obtained With Two Different Runs (a and b) for the Geoid Anomalies 1 and 2

Parameter	Mean _{1a}	Mean _{1b}	Std _{1a}	Std _{1b}	Mean _{2a}	Mean _{2b}	Std _{2a}	Std _{2b}
$\delta\rho$ (kg m ⁻³)	24	26	12	12	27	28	12	12
δX (km)	70	66	41	44	102	101	50	48
δY (km)	56	61	37	40	109	103	49	49
θ (deg)	87	87	54	55	88	89	53	53
Z_1 (km)	26	28	22	23	64	61	23	23
Z_2 (km)	70	70	35	35	120	115	33	35

4.2. Statistical Representation of Density Perturbations

For each of the observed geoid anomalies investigated here, the distribution of MCMC solutions is represented in Figure 7. The a priori bounds on model parameters are summarized in Table 1 and discussed in section 3.3. We explore a range of density from 0 to 50 kg m⁻³ for the positive geoid anomalies and from -50 to 0 kg m⁻³ for the negative anomaly. A positive density anomaly in the subsurface could lead to a negative geoid anomaly, if mantle flow associated with the density anomaly results in topographic depression. The investigated geoid anomalies are, however, not related to particular topography signatures (Figure 3), so a positive density anomaly gives rise to a positive geoid anomaly and vice versa. As most of these distributions deviate considerably from the Gaussian distribution, we calculate not only the mean and the standard deviation but also the median and interquartile range (IQR), which is defined as the difference between the first quartile and the third quartile (Table 3).

The normalized χ^2 are clustered around 1, indicating that the geoid anomalies are well fitted by the prism models selected by the MCMC procedure. As expected, the distribution of model parameters closely reflects the characteristics of geoid anomalies, i.e., their size, shape, orientation, and amplitude. For example, lateral extents δX and δY are clustered around the lower bound for smaller anomalies (e.g., anomaly 1), whereas they spread toward the upper bound for larger anomalies (e.g., anomaly 4). For all of anomalies, Z_2 is well constrained since the MCMC solutions are clustered around a specific value. A similar comment can be made for the distribution of Z_1 for the anomalies 4 and 5. For both of these anomalies, θ favors particular values (one or two modes), which explains that the lateral extents δX and δY are also well restricted around preferential values (see Appendix A). The δX and δY are also better constrained for the anomaly 1 than for the anomalies 2 and 3. The $\delta\rho$ is much more loosely constrained than the total mass δm because of the strong trade-off between the density of the prism and its geometry, as we describe below.

Table 3. Statistical Representation of MCMC Solutions for the Geoid Anomalies 1 to 5

	χ^2/ν	$\delta\rho$ (kg m ⁻³)	δX (km)	δY (km)	θ (deg)	Z_1 (km)	Z_2 (km)	δm ($\times 10^{15}$ kg)
Mean ₁	1	24	70	56	87	26	70	2.3
Median ₁	1	22	70	56	86	40	91	2.9
Std ₁	0.3	12	41	37	54	22	35	1.5
IQR ₁	0.5	21	73	60	90	47	62	2.9
Mean ₂	1.5	27	102	109	88	64	120	11.4
Median ₂	1	27	92	101	84	65	118	10.8
Std ₂	1.4	12	50	49	53	23	33	4.8
IQR ₂	1.4	20	85	83	93	40	47	7.6
Mean ₃	1	28	118	111	94	68	125	14.2
Median ₃	0.9	28	116	107	98	68	126	13.3
Std ₃	0.4	12	48	47	52	20	32	4.9
IQR ₃	0.5	19	77	78	88	33	51	7.3
Mean ₄	1.2	-32	136	142	82	53	122	-37.1
Median ₄	1.1	-33	142	141	88	55	126	-34.9
Std ₄	0.4	11	47	45	52	26	37	18.2
IQR ₄	0.5	17	63	74	97	37	49	24.9
Mean ₅	1	33	105	195	88	95	180	51.2
Median ₅	1	31	108	193	89	95	175	48.7
Std ₅	0.1	9	38	5	9	4	13	5.5
IQR ₅	0.1	16	64	10	17	8	25	9.5

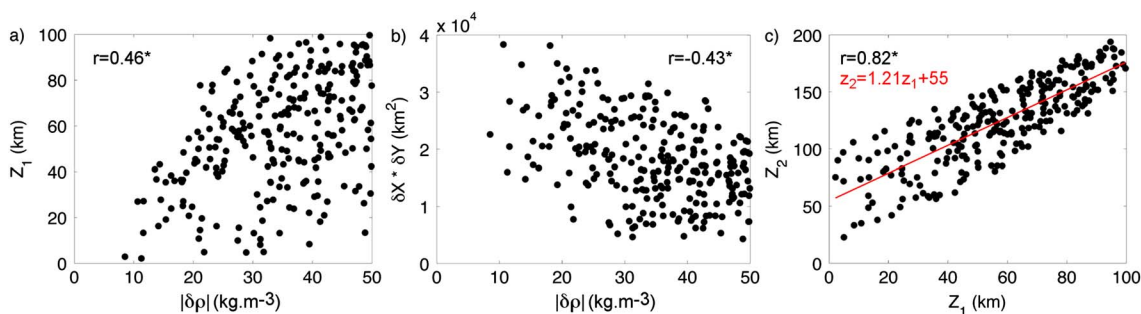


Figure 9. Scatter plot of (a) density contrast ($\delta\rho$) versus top depth (Z_1), (b) density contrast ($\delta\rho$) versus area formed by δX and δY , (c) top depth (Z_1) versus bottom depth (Z_2) for anomaly 4. Correlation coefficients are given for all panels, and for Figure 9c, the result of linear regression is also shown in red.

Certain model parameters can strongly correlate to each other (Figure 9). We use the anomaly 4 as an example; the relationships discussed here are also applicable to other anomalies. As expected from potential field theory, the amplitude of a geoid anomaly is inversely proportional to the depth of the source density anomaly. In order to counteract such signal attenuation with the source depth, $|\delta\rho|$ linearly increases with Z_1 in the inversion (Figure 9a). Figure 9b shows that $|\delta\rho|$ is also inversely correlated with the lateral extent of a source body, spanned by δX and δY . This correlation reflects that a smaller body with a high-density contrast can yield a similar result to a larger body with a low-density contrast. Another high correlation exists between Z_1 and Z_2 (Figure 9c). Linear regression yields a slope of ~ 1.2 , indicating that the vertical extent of the prism slightly increases with the depth. Again, this is to compensate signal attenuation with increasing depth.

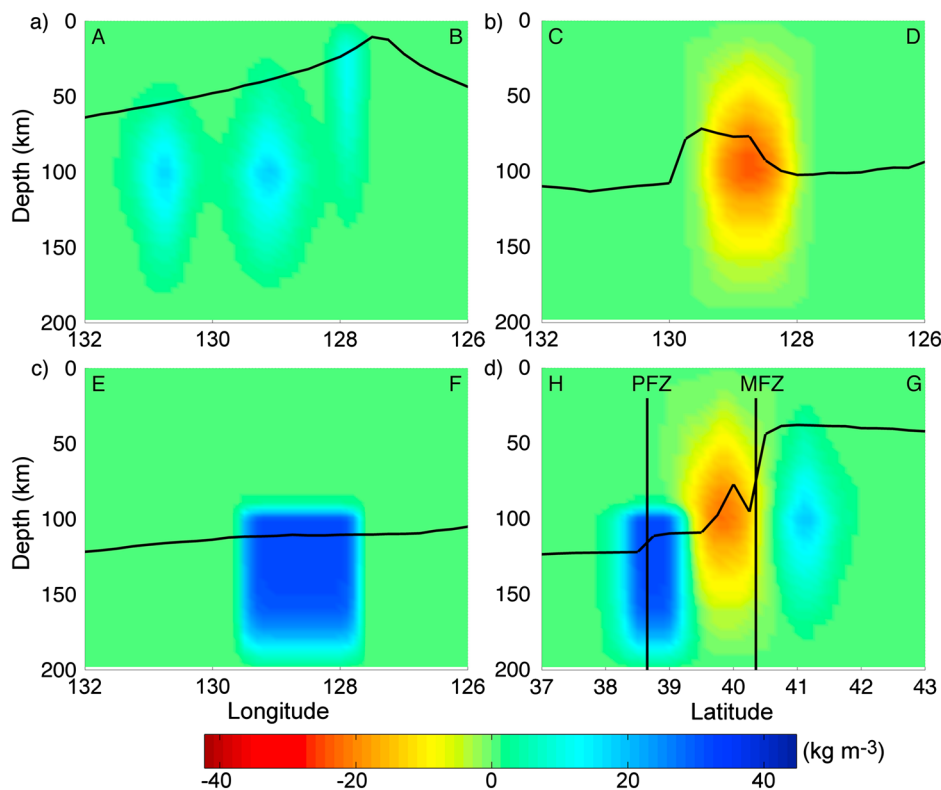


Figure 10. Depth cross sections of density anomalies, based on the mean of resampled MCMC solutions for localized geoid anomalies. Locations of cross sections are shown in Figure 2d. In each panel, black line represents the bottom of thermal lithosphere based on the half-space model. In Figure 10d, the locations of fracture zones (MFZ for Mendocino and PFZ for Pioneer) are indicated by vertical lines.

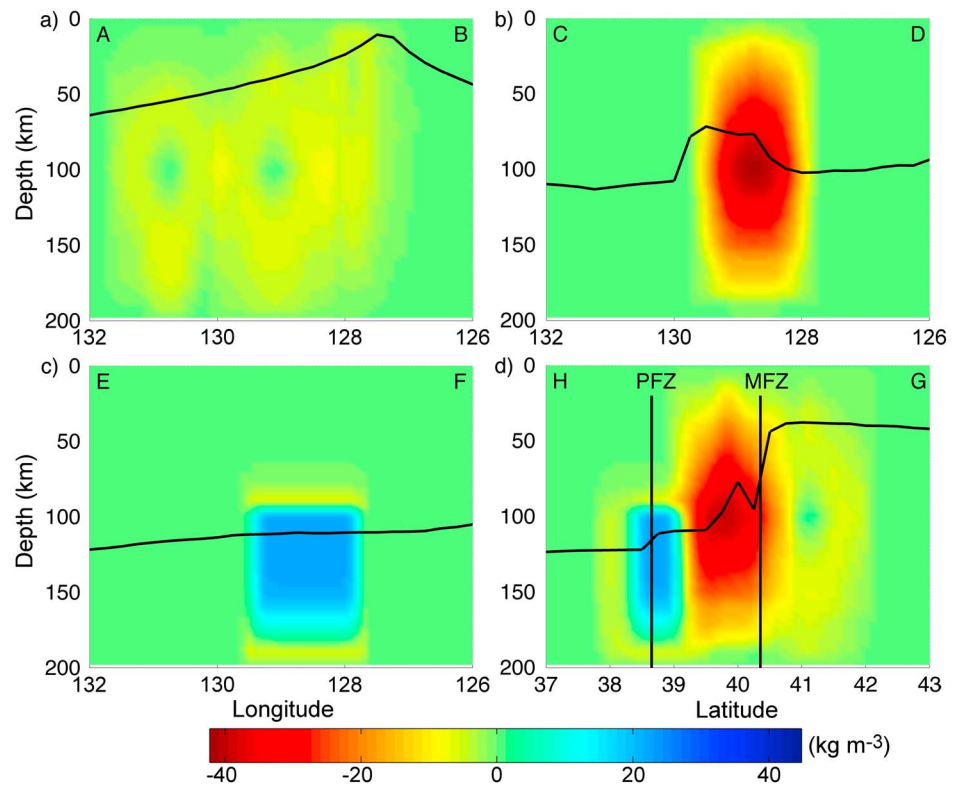


Figure 11. Same as Figure 10 but showing the lower bound of the 68% confidence limit.

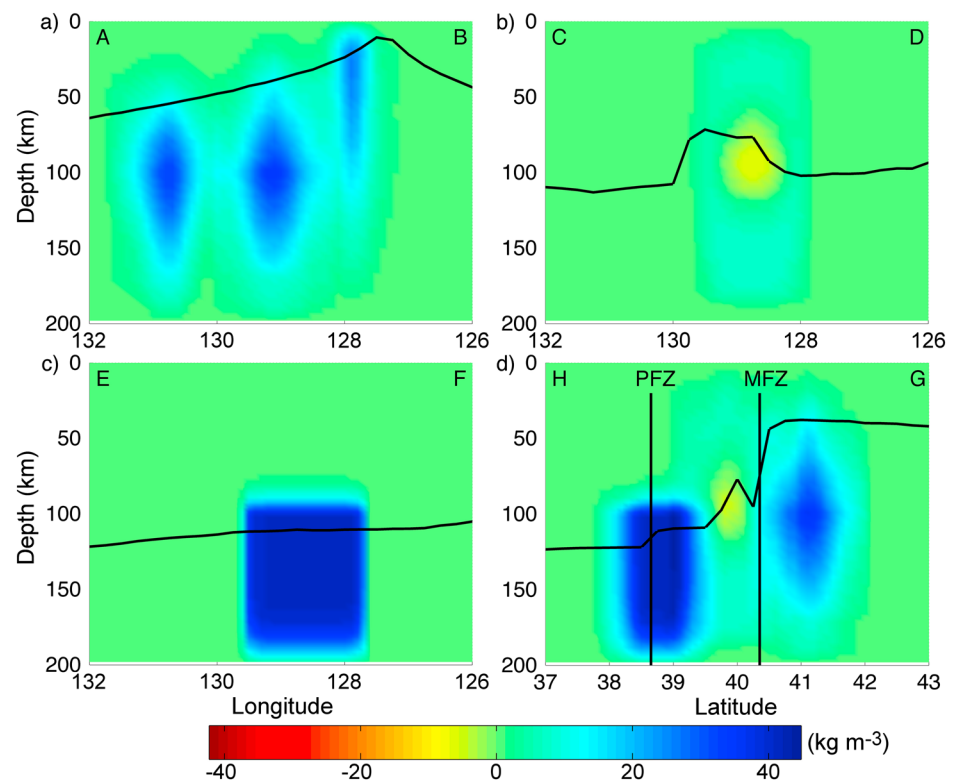


Figure 12. Same as Figure 10 but showing the upper bound of the 68% confidence limit.

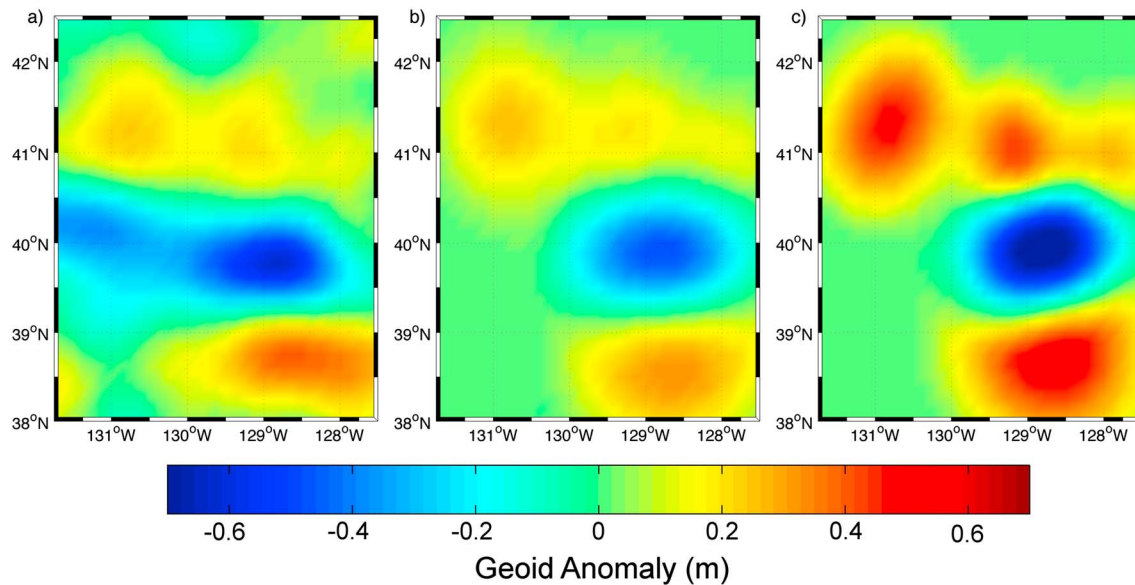


Figure 13. (a) The five observed geoid anomalies around the Mendocino Fracture Zone investigated in this study, (b) Synthetic geoid anomalies derived from the mean density distribution shown in Figure 10 and associated with χ^2 of ~ 1 , (c) Synthetic geoid anomalies calculated from prism models leading to a poor fit. Normalized χ^2 is 6, 10, 5, 7, and 5 for the anomalies 1 to 5, respectively.

The MCMC solutions are distributed over the six-dimensional model space, and to visualize these solutions succinctly, we construct a corresponding ensemble of subsurface density perturbations and calculate its statistics. As most of the distributions do not follow a Gaussian distribution, it is better to use the median and the IQR instead of the mean and the standard deviation. However, after translating the six-dimensional model space into the corresponding three-dimensional space of density perturbation, the use of median and IQR becomes inadequate; when certain points in the density space are not always covered by any of the prisms, the median for those points is likely to be biased to zero. Thus, even though plotting the mean and the standard deviation is not quite appropriate, it remains the most reasonable way to represent all solutions in the same graphic. Figure 10 shows four depth cross sections of the mean density perturbation below the five geoid anomalies. To visualize model uncertainty, the 68% confidence limit (corresponding to 1 standard deviation) is shown in Figures 11 (upper limit) and 12 (lower limit). The base of thermal lithosphere (defined at which the temperature reaches the 99% of internal temperature) predicted from the HSC model is also shown as a solid curve in each panel. On the northern side of the Mendocino Fracture Zone (i.e., on the younger side), the density perturbations are all positive and do not exceed 15 kg m^{-3} (Figures 10a and 10d). They are regularly spaced along the fracture zone, and their minimal depth follows the base of the lithosphere. Greater density perturbations are seen on the older side, reaching up to 32 kg m^{-3} for the positive anomaly and -24 kg m^{-3} for the negative anomaly (Figure 10b-d). The negative anomaly is located near the Mendocino Fracture Zone but is slightly shifted to its older side. The most positive anomaly is seen right beneath the Pioneer Fracture Zone. All of these density perturbations are located in the vicinity of the base of thermal lithosphere. In Figure 13b, we represent the geoid anomalies derived from these mean density perturbations and for which χ^2 is ~ 1 . For comparison, Figure 13c shows the geoid anomalies produced by prism models with high χ^2 .

5. Discussion

5.1. Comparison with Previous Studies

Various strategies have been proposed to deal with the nonuniqueness of potential field inversion. First of all, being nonunique is not equivalent to being totally unconstrained and it is possible to deduce some crude measure of a source, such as bounds on its depth, by considering the spectral content of gravity data [e.g., Gerard and Debeglia, 1975]. Depth resolution can be refined by considering 3-D gravity data set collected at multiple altitudes [e.g., Fedi and Rapolla, 1999] or by using spatio-spectral localization techniques in the planar case [e.g., Moreau et al., 1999; Sailhac and Gibert, 2003] or on the sphere [e.g., Simons et al.,

1997; Holschneider *et al.*, 2003; Simons *et al.*, 2006], which allows us to isolate different signal components and better localize sources at various depths.

In this study, the source characteristics are constrained by exploiting the spectral content of gravity in two different ways. First, we use geoid instead of gravity, thereby focusing on long-wavelength components. This allows us to avoid the tendency of gravity inversions to concentrate density variations near the surface and thus better interpret sources at depth. Second, the depth resolution is further refined by the continuous wavelet transform (at the scale of 100 km), by which we are able to concentrate on the upper 150 km of the mantle.

The use of a priori information, however, remains essential to overcome the inherent ambiguity of potential field inversion. Common practices include inverting for a homogeneous source of known shape [e.g., Roy, 1962; Pedersen, 1979] and solving for variations in an interface with constant density contrast [e.g., Pilkington and Crossley, 1986]. The interface approach has further been developed in the Fourier domain for terrain correction [e.g., Xia and Sprowl, 1992; Parker, 1996] and more recently in the spherical geometry [Tsoulis and Stary, 2005]. Density variation may be also prescribed as a function of depth, as usually done when solving for the thickness of a sedimentary basin [e.g., Oldenburg, 1974; Chai and Hinze, 1988]. It is also possible to invert for lateral density variations if interface geometry is known [e.g., Korenaga *et al.*, 2001]. For more complicated 3-D density distributions, inversion algorithms may incorporate different types of a priori information based on other geophysical and geological surveys [e.g., Gallardo-Delgado *et al.*, 2003; Fulla *et al.*, 2009]. In this study, in addition to assuming prisms with constant density, we consider a priori bounds on geologically realistic density contrasts that can be achieved by thermal or chemical variations in the Earth's mantle. The density perturbations resolved by our inversion scheme, therefore, not only fit the geoid data but also are well disposed for geological interpretations.

5.2. Interpretation of Inversion Results

Beneath old seafloor, the gravitational instability of a thickened thermal boundary layer could develop into small-scale convection (SSC), which is characterized by convective rolls aligned with plate motion [Richter, 1973; Richter and Parsons, 1975]. SSC may develop even under young seafloor if mantle viscosity is low enough [Buck and Parmentier, 1986; Korenaga and Jordan, 2003] or there exists lateral density variation due to a fracture zone [Huang *et al.*, 2003; Dumoulin *et al.*, 2005]. The depth and vertical extents of density anomalies derived from our inversion indicate that these anomalies are intimately related to the structure of lowermost lithosphere, pointing to the presence of SSC in the vicinity of the Mendocino Fracture Zone (Figure 14).

When SSC takes place, cold downwellings lead to the local thickening of lithosphere, resulting in positive density perturbations. Such positive perturbations can be seen on both sides of the Mendocino Fracture Zone with a ~ 200 km space between them, which is in agreement with the spatial organization of SSC in some numerical simulations [e.g., Huang *et al.*, 2003; Dumoulin *et al.*, 2005, 2008]. The thickening of lithosphere in one place induces the thinning of lithosphere in other places, resulting in the partial replacement of lithosphere with hot asthenosphere. The combined effect of a positive thermal anomaly (~ 200 – 300°C) and the thinning of lithosphere can explain remarkably well the negative density perturbation resolved under the anomaly 4.

SSC can induce melting by disrupting the thermal and compositional stratification of the uppermost mantle. The positive thermal anomalies in SSC upwellings are usually insufficient to trigger melting in a depleted harzburgite layer, which already experienced mid-ocean ridges melting. However, immediately after its onset, SSC removes this depleted layer in downgoing sheets and replaces it with fresh mantle from below, allowing subsequent melting. With normal potential temperature (i.e., $\sim 1350^\circ\text{C}$), upwelling mantle exceeds its dry solidus at the depth of 70 km and starts to melt [e.g., Langmuir *et al.*, 1992]. Our inversion result for anomaly 4 suggests that lithosphere may be thinned down to ~ 50 km (Figure 10). The vertical extent for partial melting is thus only 20 km, for which the average degree of partial melting would be 2–3%. The total amount of melt that could be produced depends on the pattern of mantle flow associated with lithospheric thinning. Melt migration through the rest of lithosphere may not be very effective because, unlike a mantle plume, upwelling due to lithospheric thinning is a one-time event. Melt generated by thinning could largely fail to reach the surface owing to its thermal interaction with cold lithosphere.

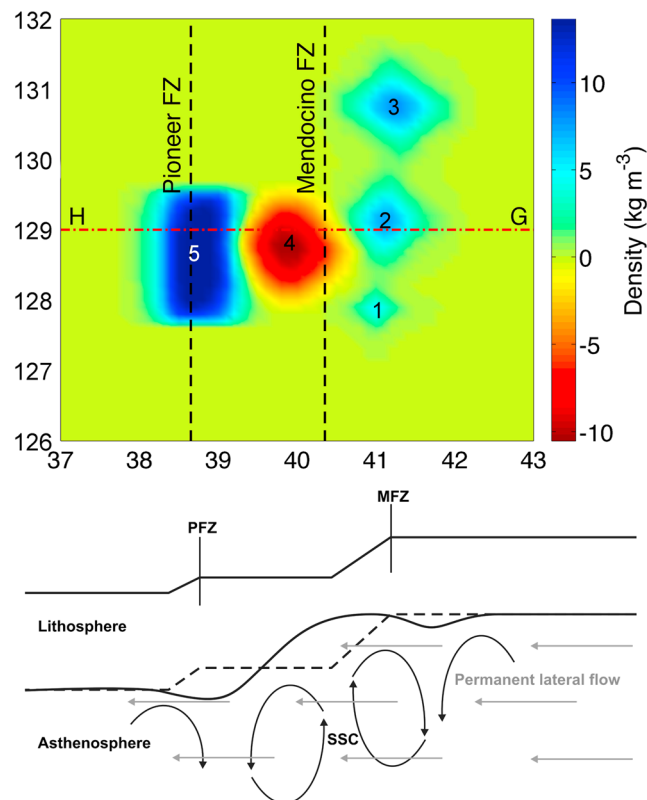


Figure 14. (top) Map of depth-averaged (from 0 to 200 km) density perturbations based on our MCMC inversion. Numbers denote corresponding geoid anomalies (Figure 2d). (bottom) Schematic illustration of small-scale convection (SSC) and its consequences on the density structure of the lithosphere. PFZ: Pioneer Fracture Zone, MFZ: Mendocino Fracture Zone.

In addition to SSC, *Dumoulin et al.* [2008] show that permanent asthenospheric flow from the younger side to the older side of a fracture zone could be driven by a lateral density variation associated with the fracture zone. This edge-driven flow thermally erodes the basal relief of the lithosphere, and as a result, a step in lithospheric thickness gradually deviates toward the older side of the fracture zone (Figure 14). This prediction is also compatible with the location of the observed negative density perturbation, which is slightly shifted to the southern side (i.e., on the older side) of the Mendocino Fracture Zone. Therefore, the deep lithospheric step does not necessarily underlie the surface fracture zone, even at young seafloor ages. The Pioneer Fracture Zone, which corresponds to a very small age offset of 3–5 Ma, displaces the ridge axis in the same direction and could slightly accentuate this phenomenon by enhancing the lateral flow velocity [*Morency et al.*, 2005]. Finally, greater density anomalies beneath the older side of the Mendocino Fracture Zone are also what is expected, because old and thus thicker lithosphere is prone to be delaminated more severely by convective instability.

5.3. Outlook

Our inversion results illustrate how the analysis of localized geoid anomalies can bring new constraints on the fine scale density structure of shallow oceanic mantle. The high precision and resolution of global geoid models allow us to apply this new approach to any area of the oceans. A global analysis of these localized anomalies will be essential to resolve the density structure of shallow oceanic mantle and should be able to identify systematics not only along fracture zones but also in other parts of ocean basins. Deviations from a reference theoretical geoid can be inverted for density perturbations to the standard model of oceanic lithosphere, which may be interpreted in terms of thermal contrasts in the convecting mantle. When combined with geodynamical studies, such temperature variations will help us to better constrain the rheology of oceanic lithosphere and asthenosphere as well. For instance, SSC with temperature variations of $\sim 200\text{--}300^\circ\text{C}$, as suggested by this study, indicates an activation energy of about 100 kJ mol^{-1} and an asthenospheric viscosity of $4 \times 10^{19}\text{--}10^{20}\text{ Pa s}$ [*Korenaga and Jordan*, 2002]. Exploiting hitherto

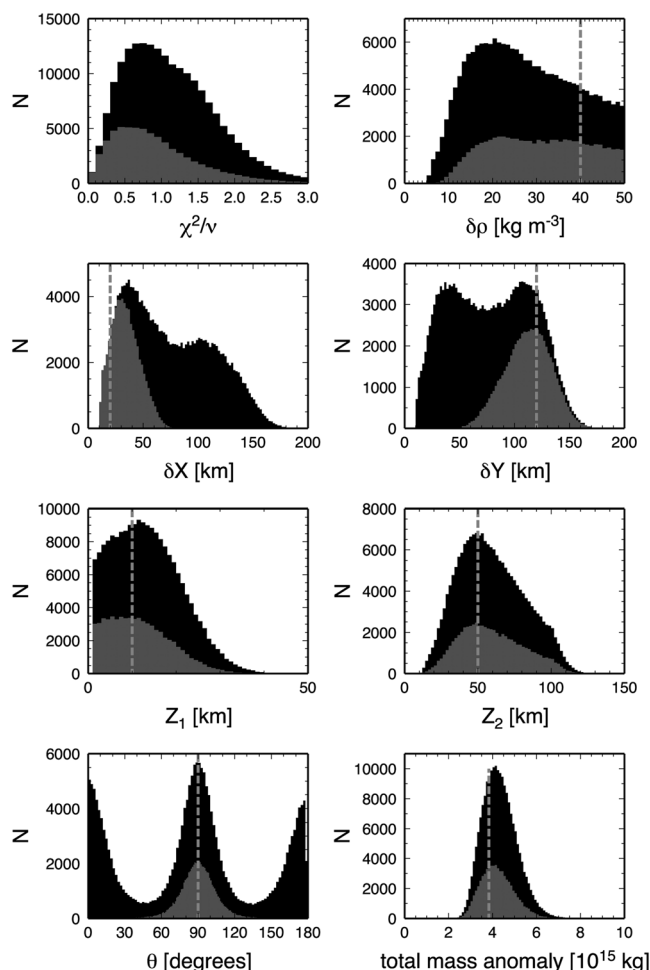


Figure A1. Histograms of MCMC solutions obtained from one simulation corresponding to a synthetic geoid anomaly. The degree of freedom ν used for normalized χ^2 is 4. The MCMC solutions for which $\delta Y > \delta X$ are represented in gray.

anomaly. The results of this inversion are shown in the Figure A1 and Table A1. To better visualize the statistical distribution of each parameter, we do not resample the MCMC solutions. We use exactly the same a priori bounds on model parameters as used in the main text.

The normalized χ^2 are clustered around 1, indicating that the synthetic geoid anomaly is well fitted by the prism models selected by the MCMC procedure. The vertical extent of the prism is particularly well recovered by the inversion since Z_1 and Z_2 are clustered around the true values. The lateral extents δX and δY have distributions with two modes: one at 40 km and another at 100–110 km. A similar observation can be made

overlooked small-scale geoid anomalies could therefore open an entirely new window into the study of mantle dynamics and serve as a bridge between experimental rock mechanics and theoretical geodynamics.

Moreover, as demonstrated in this study, the inversion of the small-scale geoid anomalies can identify local thinning/thickening of the lithosphere and thus can inform us on the structure of lithosphere-asthenosphere boundary (LAB) and its evolution. Although receiver functions allow the mapping of the oceanic LAB at a global scale [Kawakatsu et al., 2009; Rychert and Shearer, 2009; Schmerr, 2012], different seismic studies sometimes lead to conflicting interpretations. Our geoid inversion may be able to provide additional constraints and help distinguishing between different origins of LAB.

Appendix A: Statistical Distribution of MCMC Solutions for a Synthetic Example

We calculate a synthetic geoid signal for a prism with the following specifications: density perturbation ($\delta\rho = 40 \text{ kg m}^{-3}$), dimensions ($\delta X = 20 \text{ km}$, $\delta Y = 120 \text{ km}$, $Z_1 = 10 \text{ km}$, $Z_2 = 50 \text{ km}$) and orientation ($\theta = 90^\circ$). Then we invert it for the statistical distribution of its source density

Table A1. Statistical Representation of MCMC Solutions for the Synthetic Anomaly (s) and Its Restricted Version (sr)

	χ^2/ν	$\delta\rho \text{ (kg m}^{-3}\text{)}$	$\delta X \text{ (km)}$	$\delta Y \text{ (km)}$	$\theta \text{ (deg)}$	$Z_1 \text{ (km)}$	$Z_2 \text{ (km)}$	$\delta m \text{ (}\times 10^{15} \text{ kg)}$
Mean _s	1.1	27	70	89	87	11	53	4
Median _s	1	27	67	79	89	13	57	4.2
Std _s	0.6	11	41	38	51	6	20	0.6
IQR _s	0.9	19	65	63	74	11	33	1
Mean _{sr}	0.9	30	35	116	90	10	54	4
Median _{sr}	0.8	30	33	113	90	11	57	4
Std _{sr}	0.6	11	13	16	9	6	19	0.6
IQR _{sr}	0.8	18	18	29	18	10	32	1

with the orientation of prism θ , for which the distribution shows two modes at 90 and 180 (or 0), respectively. These bimodal distributions result from the rotation that perturbs the initial definition of δX and δY : the model combining a large δY and a small δX with $\theta = 90$ share the same configuration than the model combining a large δX and a small δY with $\theta = 0$ or 180. This is illustrated in Figure A1 where we show in gray the MCMC solutions for which $\delta Y > \delta X$. In this case, δX , δY , and θ present a unimodal distribution and are clustered around the true value.

The statistical distribution of $\delta \rho$ shows a mode at $\sim 20 \text{ kg m}^{-3}$, which is far below the true value of 40 kg m^{-3} . By imposing more constraints on the geometry of the prism, the unimodal distribution disappears and the MCMC solutions spread toward the larger density values. The difficulty to perfectly recover the density is explained by the strong trade-off between the density of the prism and its geometry. This is confirmed by plotting the distribution of the total mass of prism, which is indeed well clustered around the true value of $3.84 \times 10^{15} \text{ kg}$.

Acknowledgments

We are grateful to two anonymous reviewers for critical and constructive comments on the manuscript. This work was supported in part by the facilities and staff of the Yale University Faculty of Arts and Sciences High Performance Computing Center.

References

- Blakely, R. J. (1995), *Potential Theory in Gravity and Magnetic Applications*, Cambridge Univ. Press, New York.
- Boyd, F. R. (1989), Compositional distinction between oceanic and cratonic lithosphere, *Earth Planet. Sci. Lett.*, *96*, 15–26.
- Buck, W. R., and E. M. Parmentier (1986), Convection beneath young oceanic lithosphere: Implications for thermal structure and gravity, *J. Geophys. Res.*, *91*, 1961–1974.
- Cadio, C., and J. Korenaga (2012), Localization of geoid anomalies and the evolution of oceanic lithosphere: A case study from the Mendocino Fracture Zone, *J. Geophys. Res.*, *117*, B10404, doi:10.1029/2012JB009524.
- Cadio, C., I. Panet, A. Davaille, M. Diament, L. Métivier, and O. de Viron (2011), Pacific geoid anomalies revisited in light of thermochemical oscillating domes in the lower mantle, *Earth Planet. Sci. Lett.*, *306*, 123–135.
- Cadio, C., M. Ballmer, I. Panet, M. Diament, and N. Ribe (2012), New constraints on the origin of the Hawaiian swell from wavelet analysis of the geoid to topography ratio, *Earth Planet. Sci. Lett.*, *359–360*, 40–54.
- Carlson, R. L., and H. P. Johnson (1994), On modeling the thermal evolution of the oceanic upper mantle: An assessment of the cooling plate model, *J. Geophys. Res.*, *99*, 3201–3214, doi:10.1029/93JB02696.
- Chai, Y., and W. J. Hinze (1988), Gravity inversion of an interface above which the density contrast varies exponentially with depth, *Geophysics*, *53*, 837–845.
- Davaille, A., and C. Jaupart (1994), Onset of thermal convection in fluids with temperature-dependent viscosity: Application to the oceanic mantle, *J. Geophys. Res.*, *99*, 19,853–19,866.
- Driscoll, M. L., and B. Parsons (1988), Cooling of the oceanic lithosphere—Evidence from geoid anomalies across the Udintsev and Eltanin fracture zones, *Earth Planet. Sci. Lett.*, *88*, 289–307.
- Dumoulin, C., M. P. Doin, L. Fleitout, and D. Arcay (2005), Onset of small scale instabilities at the base of the lithosphere: Scaling laws and role of pre-existing lithospheric structures, *Geophys. J. Int.*, *160*, 344–356.
- Dumoulin, C., G. Choblet, and M. P. Doin (2008), Convective interactions between oceanic lithosphere and asthenosphere: Influence of a transform fault, *Earth Planet. Sci. Lett.*, *274*, 301–309.
- Fedi, M., and A. Rapolla (1999), 3-D inversion of gravity and magnetic data with depth resolution, *Geophysics*, *64*, 452–460.
- Freedman, A. P., and B. Parsons (1990), Geoid anomalies over two South Atlantic fracture zones, *Earth Planet. Sci. Lett.*, *100*, 18–41.
- Förste, C., et al. (2008), The GeoForschungsZentrum Potsdam/Groupe de Recherche de Géodésie Spatiale satellite-only and combined gravity field models: EIGEN-GL04S1 and EIGEN-GL04C, *J. Geod.*, *82*, 331–346, doi:10.1007/s00190-007-0183-8.
- Fuller, J., J. C. Afonso, J. A. D. Connolly, M. Fernández, D. García-Castellanos, and H. Zeyen (2009), LitMod3D: An interactive 3-D software to model the thermal, compositional, density, seismological, and rheological structure of the lithosphere and sublithospheric upper mantle, *Geochem. Geophys. Geosyst.*, *10*, Q08019, doi:10.1029/2009GC002391.
- Gallardo-Delgado, L. A., M. A. Pérez-Flores, and E. Gómez-Treviño (2003), A versatile algorithm for joint 3D inversion of gravity and magnetic data, *Geophysics*, *68*(3), 949–959.
- Gerard, A., and N. Debeglia (1975), Automatic three-dimensional modeling for the interpretation of gravity or magnetic anomalies, *Geophysics*, *40*, 1014–1034.
- Hall, C. E., and M. Gurnis (2005), Strength of fracture zones from their bathymetric and gravitational evolution, *J. Geophys. Res.*, *110*, B01402, doi:10.1029/2004JB003312.
- Hastings, W. K. (1970), Monte Carlo sampling methods using Markov chains and their applications, *Biometrika*, *57*, 97–109.
- Haxby, W. F., and D. L. Turcotte (1978), On isostatic geoid anomalies, *J. Geophys. Res.*, *83*, 5473–5478.
- Herzberg, C., P. D. Asimow, N. Arndt, Y. Niu, C. M. Lesher, J. G. Fittton, M. J. Cheadle, and A. D. Saunders (2007), Temperatures in ambient mantle and plumes: Constraints from basalts, picrites, and komatiites, *Geochem. Geophys. Geosyst.*, *8*, Q02006, doi:10.1029/2006GC001390.
- Holschneider, M., A. Chambodut, and M. Manda (2003), From global to regional analysis of the magnetic field on the sphere using wavelet frames, *Phys. Earth Planet. Inter.*, *135*, 107–124.
- Huang, J., S. Zhong, and J. van Hunen (2003), Controls on sublithospheric small-scale convection, *J. Geophys. Res.*, *108*, 2405, doi:10.1029/2003JB002456.
- Kawakatsu, H., P. Kumar, Y. Takei, M. Shinohara, T. Kanazawa, E. Araki, and K. Suyehiro (2009), Seismic evidence for sharp lithosphere-asthenosphere boundaries of oceanic plates, *Science*, *324*(5926), 499–502, doi:10.1126/science.1169499.
- Korenaga, J., and T. H. Jordan (2002), On 'steady-state' heat flow and the rheology of oceanic mantle, *Geophys. Res. Lett.*, *29*(22), 2056, doi:10.1029/2002GL016085.
- Korenaga, J., and T. H. Jordan (2003), Physics of multiscale convection in Earth's mantle: Onset of sublithospheric convection, *J. Geophys. Res.*, *108*(B7), 2333, doi:10.1029/2002JB001760.
- Korenaga, T., and J. Korenaga (2008), Subsidence of normal oceanic lithosphere, apparent thermal expansivity, and seafloor flattening, *Earth Planet. Sci. Lett.*, *268*, 41–51.
- Korenaga, J., W. S. Holbrook, R. S. Detrick, and P. B. Kelemen (2001), Gravity anomalies and crustal structure at the southeast Greenland margin, *J. Geophys. Res.*, *106*, 8853–8870.

- Langmuir, C. H., E. M. Klein, and T. Plank (1992), Petrological systematics of mid-ocean ridge basalts: Constraints on melt generation beneath ocean ridges, in *Mantle Flow and Melt Generation at Mid-Ocean Ridges*, edited by J. Phipps Morgan, D. K. Blackman, and J. M. Sinton, pp. 183–280, AGU, Washington, D. C.
- Lee, C.-T. A. (2004), Compositional variation of density and seismic velocities in natural peridotites at STP conditions: Implications for seismic imaging of compositional heterogeneities in the upper mantle, *J. Geophys. Res.*, *108*(B9), 2441, doi:10.1029/2003JB002413.
- Liu, J. S. (2001), *Monte Carlo Strategies in Scientific Computing*, Springer, New York.
- Lyubetskaya, T., and J. Korenaga (2007), Chemical composition of Earth's primitive mantle and its variance, 1, Method and results, *J. Geophys. Res.*, *112*, B03211, doi:10.1029/2005JB004223.
- Marty, J., and A. Cazenave (1988), Thermal evolution of the lithosphere beneath fracture zones inferred from geoid anomalies, *Geophys. Res. Lett.*, *15*, 593–596.
- Metropolis, N., A. W. Rosenbluth, M. N. Rosenbluth, A. H. Teller, and E. Teller (1953), Equation of state calculations by fast computing machines, *J. Chem. Phys.*, *21*, 1087–1091.
- Moreau, F., D. Gibert, M. Holschneider, and G. Saracco (1999), Identification of sources of potential fields with the continuous wavelet transform: Basic theory, *J. Geophys. Res.*, *104*, 5003–5013.
- Morency, C., M. P. Doin, and C. Dumoulin (2005), Three-dimensional numerical simulations of mantle flow beneath mid-ocean ridges, *J. Geophys. Res.*, *110*, B11407, doi:10.1029/2004JB003454.
- Mosegaard, K., and A. Tarantola (1995), Monte Carlo sampling of solutions to inverse problems, *J. Geophys. Res.*, *100*, 12,431–12,447.
- Müller, R. D., M. Sdrolias, C. Gaina, and W. R. Roest (2008), Age, spreading rates, and spreading asymmetry of the world's ocean crust, *Geochem. Geophys. Geosyst.*, *9*, Q04006, doi:10.1029/2007GC001743.
- Nagy, D., G. Papp, and J. Benedek (2000), The gravitational potential and its derivatives for the prism, *J. Geod.*, *74*, 552–560.
- Ockendon, J. R., and D. L. Turcotte (1977), On the gravitational potential and field anomalies due to thin mass layers, *Geophys. J. R. Astron. Soc.*, *48*, 479–492.
- Oldenburg, D. W. (1974), The inversion and interpretation of gravity anomalies, *Geophysics*, *39*, 394–408.
- Parker, R. L. (1972), The rapid calculation of potential anomalies, *Geophys. J. R. Astron. Soc.*, *31*, 447–455.
- Parker, R. L. (1996), Improved Fourier terrain correction II, *Geophysics*, *61*, 365–372.
- Parsons, B., and J. G. Sclater (1977), An analysis of the variation of ocean floor bathymetry and heat flow with age, *J. Geophys. Res.*, *82*, 803–827, doi:10.1029/JB082i005p00803.
- Parsons, B., and F. M. Richter (1980), A relation between driving forces and geoid anomaly associated with mid-ocean ridges, *Earth Planet. Sci. Lett.*, *51*, 445–450.
- Pedersen, L. B. (1979), Constrained inversion of potential field data, *Geophys. Prosp.*, *27*, 726–748.
- Phipps Morgan, J., W. J. Morgan, and E. Price (1995), Hotspot melting generates both hotspot volcanism and a hotspot swell?, *J. Geophys. Res.*, *100*, 8045–8062.
- Pilkington, M., and D. J. Crossley (1986), Determination of crustal interface topography from potential fields, *Geophysics*, *51*, 1277–1284.
- Press, W. H., S. A. Teukolsky, W. T. Vetterling, and B. P. Flannery (1992), *Numerical Recipes in C*, 2nd ed., Cambridge Univ. Press, New York.
- Ribe, N. M., and U. R. Christensen (1994), Three-dimensional modeling of plume-lithosphere interaction, *J. Geophys. Res.*, *99*, 669–682.
- Richter, F. M. (1973), Convection and large-scale circulation of the mantle, *J. Geophys. Res.*, *78*, 8735–8745.
- Richter, F. M., and B. Parsons (1975), On the interaction of two scales of convection in the mantle, *J. Geophys. Res.*, *80*, 2529–2541.
- Ritzwoller, M. H., N. M. Shapiro, and S. Zhong (2004), Cooling history of the Pacific lithosphere, *Earth Planet. Sci. Lett.*, *226*, 69–84.
- Robert, C. P., and G. Cassella (2004), *Monte Carlo Statistical Methods*, Springer, New York.
- Robinson, E. M., B. Parsons, and M. Driscoll (1988), The effect of a shallow low-viscosity zone on the mantle flow, the geoid anomalies and the geoid and depth-age relationships at fracture zones, *Geophys. J.*, *93*, 25–43.
- Roy, A. (1962), Ambiguity in geophysical interpretation, *Geophysics*, *28*, 90–99.
- Rychert, C. A., and P. M. Shearer (2009), A global view of the lithosphere-asthenosphere boundary, *Science*, *324*(5926), 495–498, doi:10.1126/science.1169754.
- Sailhac, P., and D. Gibert (2003), Identification of sources of potential fields with the continuous wavelet transform: Two-dimensional wavelets and multipolar approximations, *J. Geophys. Res.*, *108*(B5), 2262, doi:10.1029/2002JB002021.
- Sandwell, D. T. (1984), Thermomechanical evolution of oceanic fracture zones, *J. Geophys. Res.*, *89*, 11,401–11,413.
- Sandwell, D. T., and G. Schubert (1980), Geoid height versus age for symmetric spreading ridges, *J. Geophys. Res.*, *85*, 7235–7241.
- Sandwell, D. T., and G. Schubert (1982), Lithospheric flexure at fracture zones, *J. Geophys. Res.*, *87*, 4657–4667.
- Schmerr, N. (2012), The Gutenberg discontinuity: Melt at the Lithosphere-Asthenosphere Boundary, *Science*, *335*, 1480–1483, doi:10.1126/science.1215433.
- Simons, M., S. C. Solomon, and B. H. Hager (1997), Localization of gravity and topography: Constraints on the tectonics and mantle dynamics of Venus, *Geophys. J. Int.*, *131*, 24–44.
- Simons, F. J., F. A. Dahlen, and M. A. Wieczorek (2006), Spatiospectral concentration on a sphere, *SIAM Rev.*, *48*, 504–536, doi:10.1137/S0036144504445765.
- Sleep, N. H. (1990), Hotspots and mantle plumes: Some phenomenology, *J. Geophys. Res.*, *95*, 6715–6736.
- Stein, C. A., and S. Stein (1992), A model for the global variation in oceanic depth and heat flow with age, *Nature*, *359*, 123–129, doi:10.1038/359123a0.
- Tarantola, A. (1987), *Inverse Problem Theory: Methods for Data Fitting and Model Parameter Estimation*, Elsevier, New York.
- Tsoulis, D., and B. Stary (2005), An isostatically compensated gravity model using spherical layer distributions, *J. Geod.*, *78*, 418–424.
- Turcotte, D. L. (1979), Flexure, *Adv. Geophys.*, *21*, 51–86.
- Turcotte, D., and G. Schubert (2002), *Geodynamics*, 2nd ed., Cambridge Univ. Press, Cambridge, U. K.
- Wessel, P., and W. F. Haxby (1989), Geoid anomalies at fracture zones and thermal models for the oceanic lithosphere, *Geophys. Res. Lett.*, *16*, 827–830.
- Xia, J., and D. R. Sprowl (1992), Inversion of potential field data by iterative forward modeling in the wavenumber domain, *Geophysics*, *57*, 126–130.
- Zhong, S., and A. B. Watts (2002), Constraints on the dynamics of mantle plumes from uplift of the Hawaiian Islands, *Earth Planet. Sci. Lett.*, *203*, 105–116.